Dual Coaxial Longitudinal Polarization Vortex Structures

Zhongsheng Man,[1,2,*] Zheng Xi,[2,*] Xiaocong Yuan,[3,†] R. E. Burge,[4] and H. Paul Urbach[2,‡]
[1]School of Physics and Optoelectronic Engineering, Shandong University of Technology, Zibo 255000, China
[2]Optics Research Group, Department of Imaging Physics, Delft University of Technology, Lorentzweg 1, 2628CJ Delft, The Netherlands
[3]Nanophotonics Research Center, Shenzhen University, Shenzhen 518060, China
[4]Cavendish Laboratory, University of Cambridge, Madingley Road, Cambridge CB3 0HE, United Kingdom

(Received 17 July 2019; accepted 19 February 2020; published 9 March 2020)

Carrying orbital angular momentum per photon, the optical vortex has elicited widespread interest. Here, we demonstrate that dual coaxial longitudinal polarization vortices can appear upon a nonparaxial propagation of a tightly focused Pancharatnam-Berry tailored Laguerre-Gaussian beam. Most importantly, it is capable of accessing arbitrary independent topological charges for both vortices, as well as predesigned tunable spacing distances between them.

DOI: 10.1103/PhysRevLett.124.103901

A light beam may possess angular momentum (AM) in addition to linear momentum [1–13]. For paraxial beams such as the Laguerre-Gaussian beams discussed in this Letter, there are two categories of AMs including spin angular momentum (SAM) and orbital angular momentum (OAM). However, for a general case, especially for the nonparaxial case, this separation becomes problematic due to the insistency to the transversality condition for photon [1,2]. Being related to the vectorial nature of light, SAM is intrinsic, having only two possible quantized values of $\pm\hbar$ depending on the handedness of the circular polarization, $\hbar$ is the reduced Planck constant, h divided by 2π [3,4]. In contrast, OAM has both intrinsic and extrinsic terms, the latter being coordinate dependent [7]. The intrinsic OAM, hereafter simply referred to as OAM, is related to the azimuthal dependence of the optical phase. When a light beam possesses a vortex phase of $\exp(il\phi)$, it can carry an optical OAM of $l\hbar$ per photon, where l is the topological charge, indicating the repeating rate of 2π phase shifts azimuthally along the beam cross section [5–13]. Such vortex beams exhibit a helical wave front and possess a phase singularity at the beam center, resulting in a doughnut-shaped intensity profile [14,15].

Since the discovery of light's OAM in the paraxial region [5], optical vortices have provided insights into the fundamental properties of light and lead to many applications, including micromanipulation [16,17], optical communication [18–23], superresolution imaging [24–26], and quantum information processing [27,28], etc. Various advances have been achieved in the creation and manipulation of optical OAM. Conventionally, OAM beams may be generated in various ways, like a spiral phase plate [29–32], computer-generated holograms [33,34], and subwavelength gratings [35]. These techniques rely on introducing a phase discontinuity in the wave front to generate beams with desired OAM modes. Under specific conditions, the intrinsic optical degree of freedom (DOF) of polarization also enables the manipulation of optical OAM states via the procedure referred to as spin-orbit coupling (SOC) [36–45]. Such processes provide a direct connection between SAM and OAM. Most recently, the conversion of arbitrary elliptically polarized states into states with independent values of OAM was also achieved [46].

When the paraxial beam is tightly focused, a strong longitudinal component appears at the focal region [47,48]. This longitudinal polarization component of light can be further structured, resulting in linked and knotted longitudinal vortex lines [49] and longitudinally polarized optical needles [50]. In addition to being of academic interest, the longitudinal field has many attractive applications, for instance, in particle acceleration, harmonic generation, fluorescent imaging, and Raman spectroscopy. It is demonstrated that, by tightly focusing an incident circularly polarized beam, a helical phase of the longitudinal component of the electric field can be created [51]. However, the topological charge of these longitudinal electric fields remains either $+1$ or -1, depending on the handedness of the incoming circular polarization; the challenge is to have access to arbitrary topological charges in the longitudinal component.

In this Letter, we demonstrate the creation of dual coaxial longitudinal polarization vortex structures with arbitrary topological charges that are spatially separated and the distance between them is tunable. To do this, we invert the problem and show how one can structure the transverse polarization and phase structures of an input field in the pupil plane to generate the vortex structures with the stated longitudinal polarization vortices. Then, we develop a rigorous analytical model to calculate the electromagnetic field and energy flow in the focal volume of the structured

input field we propose. Finally, we apply this method and present the first examples of dual coaxial longitudinal optical vortices with the same topological charge.

Polarization, as an intrinsic optical DOF, is one of the salient features of light. In addition to being the simplest and most fundamental homogenous states of polarization, a light beam admits spatially inhomogeneous states of polarization, the so-called vector optical field [52–55]. From theory, light with an arbitrary locally linear state of polarization (SOP) is expressed as

$$\mathbf{E}_o = A_0(r,\phi) \times [\cos\delta(r,\phi)\hat{\mathbf{e}}_{x_0} + \sin\delta(r,\phi)\hat{\mathbf{e}}_{y_0}], \quad (1)$$

where A_0 denotes the complex amplitude and δ specifies the orientation. The local SOP in the beam cross section of the light given in Eq. (1) is linearly polarized, because the orthogonal base vectors in terms of x_0 and y_0 components are always in phase. Using the relations $\hat{\mathbf{e}}_{x_0} = (\hat{\mathbf{e}}_r + \hat{\mathbf{e}}_l)/\sqrt{2}$ and $\hat{\mathbf{e}}_{y_0} = i(\hat{\mathbf{e}}_r - \hat{\mathbf{e}}_l)/\sqrt{2}$, Eq. (1) is also representable in terms of orthogonal circularly polarized base vectors,

$$\mathbf{E}_o = \frac{A(r,\phi)}{\sqrt{2}} \times \{\exp[-i\delta(r,\phi)]\hat{\mathbf{e}}_l + \exp[i\delta(r,\phi)]\hat{\mathbf{e}}_r\}, \quad (2)$$

where $\hat{\mathbf{e}}_l$ and $\hat{\mathbf{e}}_r$ are the respective left- (LH) and right-hand (RH) circularly polarized unit vectors. Therefore, any local linear vibration can be viewed as the superposition of two circular vibrations that have opposite handedness and carry opposite Pancharatnam-Berry (PB) phases [56,57]. Hence, achieving and observing double SOCs is possible if we can ensure the two states of the LH and RH SOCs are spatially separated.

To produce the dual coaxial longitudinal polarization vortex structures, a high-NA objective lens is introduced (Fig. 1). Tight focusing is highly desirable, ranging from microimaging to optical manipulation and high-density storage. In such systems, the optical field in the image space should be analyzed using vectorial diffraction theory [58], because the contribution of the input polarization cannot be neglected. According to the Richards and Wolf vectorial diffraction theory, the electric field near the focus of arbitrary polarized beam is given by a diffraction integral [58],

$$\boldsymbol{E}_i = \frac{-ik}{2\pi}\iint_{\Omega} a \times \exp[ik(s\cdot r)]d\Omega, \quad (3)$$

where k is the wave number in image space, $\mathbf{a}$ is the strength vector that is related to the electric field in object space, $\boldsymbol{s} = (\sin\theta\cos\varphi_{\mathbf{s}}, \sin\theta\sin\varphi_{\mathbf{s}}, \cos\theta)$ is the unit vector along a typical ray in image space, $\boldsymbol{r}$ is the radius vector of arbitrary point $P(\rho,\varphi,z)$ in image space, and Ω is the solid angle formed by all the geometrical rays that pass

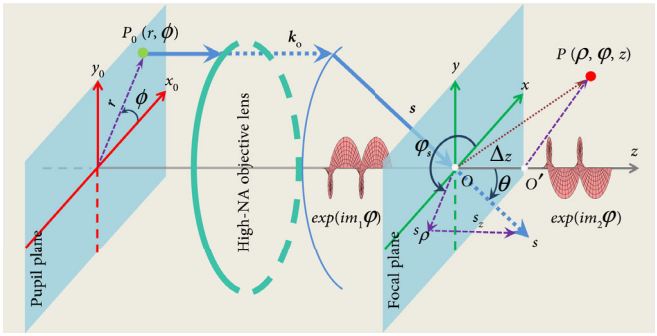

FIG. 1. Schematic of the creation of dual coaxial longitudinal polarization vortex structures and geometry, as well as the coordinate system followed in our calculations. The focal plane is located at $z = 0$. A carefully tailored Laguerre-Gaussian distribution $\mathrm{LG}_{(l,p)}$ input light with Pancharatnam-Berry phase, propagating along the z axis is incident on a high-NA objective lens (NA = 0.95), which acts as a modulator that enables the two components of RH and LH circular vibrations of the input beam to be focused to different predesigned locations on the axis. Hence, twin foci along the optical axis are obtained, resulting in helical phases with arbitrary topological charges for the longitudinal field of each focus.

through the exit pupil of the system. When the focus is located at the origin $O(0,0,0)$, for an arbitrary point P near the focus in the image region and considering $\varphi_{\mathbf{s}} = \pi + \phi$, where ϕ is the azimuthal angle with respect to the x_0 axis in the object space, we have

$$\boldsymbol{s}\cdot\boldsymbol{r} = -\rho\sin\theta\cos(\phi-\varphi) + z\cos\theta. \quad (4)$$

In contrast, when the focus is shifted to another position $O'(0,0,\Delta z)$ along the optical axis by radius vector $\boldsymbol{r}_{OO'} = (0,0,\Delta z)$, considering the spatial translation invariance of the focus, $\boldsymbol{s}\cdot\boldsymbol{r}$ in Eq. (3) is modified to

$$\begin{aligned}\boldsymbol{s}\cdot(\boldsymbol{r}-\boldsymbol{r}_{OO'}) &= \boldsymbol{s}\cdot\boldsymbol{r} - \boldsymbol{s}\cdot\boldsymbol{r}_{OO'} \\ &= -\rho\sin\theta\cos(\phi-\varphi) + z\cos\theta - \Delta z\cos\theta.\end{aligned} \quad (5)$$

Physically, the input field is now modulated by an additional phase, compared with the situation without shifting. When the high-NA objective lens obeys the sine condition, the corresponding phase distribution in the input pupil plane becomes

$$\chi = -k\Delta z\sqrt{1-\left(\frac{rNA}{r_0 n}\right)^2}, \quad (6)$$

where NA and n are the numerical aperture of the objective lens and the refractive index in image space, and r and r_0 denote the polar radius in the polar system and radius of the input optical field.

From theory, when δ in Eq. (2) has the form $\delta = \chi + m\phi$, where m is the azimuthal index, the two components of the RH and LH vibrations are focused on different locations, $(0, 0, \Delta z)$ and $(0, 0, -\Delta z)$, respectively, which are points of symmetry. As a result, this enables the two components of LH and RH SOCs to be spatially separated. Furthermore, we are able to generate arbitrary values for the optical OAM. To verify the theoretical prediction, we employ the Laguerre-Gaussian distribution $\mathrm{LG}_{(l,p)}$ input field with the polarizations constructed above, where l and p are the numbers of intertwined helices known as the topological charge and the additional concentric rings. With $p = 0$, the electromagnetic field in the image space of the strongly focused $\mathrm{LG}_{(l,0)}$ input field in the pupil plane becomes

$$\begin{bmatrix} \boldsymbol{E} \\ \boldsymbol{H} \end{bmatrix} = -\frac{ikf}{2\pi}\int_0^{\alpha}\int_0^{2\pi} \sqrt{\cos\theta}\, e^{\{ik[-\rho\sin\theta\cos(\phi-\varphi)+z\cos\theta]\}} \times \left(\frac{\sqrt{2}\beta\sin\theta}{\sin\alpha}\right)^{|l|} e^{\left(-\frac{\beta^2\sin^2\theta}{\sin^2\alpha}\right)} e^{(il\phi)} \begin{bmatrix} \boldsymbol{V}_E \\ \boldsymbol{V}_H \end{bmatrix} \sin\theta d\phi d\theta, \tag{7}$$

where f is the focal distance, $\alpha = \arcsin(\mathrm{NA}/n)$ is the maximum aperture angle, and β is the ratio of the pupil radius to the beam waist that we take as one in the following calculations. The vectors $\boldsymbol{V}_E$ and $\boldsymbol{V}_H$ represent the electric and magnetic field polarization vectors in the image space with the three mutually perpendicular components being

$$\begin{aligned} \boldsymbol{V}_{Ex} &= \sin(\phi - T)\sin\phi + \cos(\phi - T)\cos\theta\cos\phi \\ \boldsymbol{V}_{Ey} &= -\sin(\phi - T)\cos\phi + \cos(\phi - T)\cos\theta\sin\phi \\ \boldsymbol{V}_{Ez} &= \cos(\phi - T)\sin\theta, \end{aligned} \tag{8}$$

$$\begin{aligned} \boldsymbol{V}_{Hx} &= A[-\cos(\phi - T)\sin\phi + \sin(\phi - T)\cos\theta\cos\phi] \\ \boldsymbol{V}_{Hy} &= A[\cos(\phi - T)\cos\phi + \sin(\phi - T)\cos\theta\sin\phi] \\ \boldsymbol{V}_{Hz} &= A[\sin(\phi - T)\sin\theta]. \end{aligned} \tag{9}$$

Here $T = -k\Delta z\cos\theta + m\phi$, and $A = \sqrt{\varepsilon/\mu}$, where ε and μ denote the permittivity and permeability, respectively.

The longitudinal component of the electric field is

$$\begin{aligned} E_z = {} & Ce^{i(l+m-1)\varphi}\int_0^{a} Be^{-ik\Delta z\cos\theta} i^{l+m-1} J_{l+m-1}(-k\rho\sin\theta)d\theta \\ & + Ce^{i(l-m+1)\varphi}\int_0^{a} Be^{ik\Delta z\cos\theta} i^{l-m+1} J_{l-m+1}(-k\rho\sin\theta)d\theta, \end{aligned} \tag{10}$$

where $B = \sqrt{\cos\theta}(\sqrt{2}\beta\sin\theta/\sin\alpha)^{|l|} e^{[-(\beta^2\sin^2\theta/\sin^2\alpha)]} e^{ikz\cos\theta}\sin^2\theta$, $C = -ikf/2$, and $J_s(-k\rho\sin\theta)$ is the Bessel function of the first kind and order s. It can be seen clearly that the longitudinal field Ez has two different phase vortices with topological charges $l + m - 1$ and $l - m + 1$, indicated by the terms $e^{i(l+m-1)\varphi}$ and $e^{i(l-m+1)\varphi}$. They are located at Δz and $-\Delta z$, respectively. By tuning l (topological charge in the incoming paraxial beam) and m (the topological charge in the PB phase at the input pupil) independently, the two topological charges of the E_z component can be tuned. Their separation $2\Delta z$ is determined by the phase modulation χ in Eq. (6). By changing χ, the spacing distance can be tuned.

In terms of the full time-dependent three-dimensional electric and magnetic fields, the energy current is defined by the time-averaged Poynting vector [58],

$$\boldsymbol{S} \propto \mathrm{Re}(\boldsymbol{E} \times \boldsymbol{H}^*), \tag{11}$$

where the asterisk denotes complex conjugation.

We first consider the $\mathrm{LG}_{(0,0)}$ beam and set χ in the input pupil according to Eq. (6) with $\Delta z = 3\lambda$ (λ is the wavelength of the incoming light) and $m = -1$ (NA = 0.95, $n = 1$). Based on the above analysis, we would expect to see two foci with topological charges $l + m - 1 = -2$ and $l - m + 1 = 2$ in the E_z component at $z = 3\lambda$ and $z = -3\lambda$, respectively. The calculated focal field distribution is shown in Fig. 2. Obviously, twin foci with nearly the same profiles for all the total [Fig. 2(a)], transverse [Fig. 2(b)], and longitudinal [Fig. 2(c)] fields are obtained. They all exhibit, moreover, twin hollow-shaped patterns with a zero field distribution on the axis. The upper focus, which is

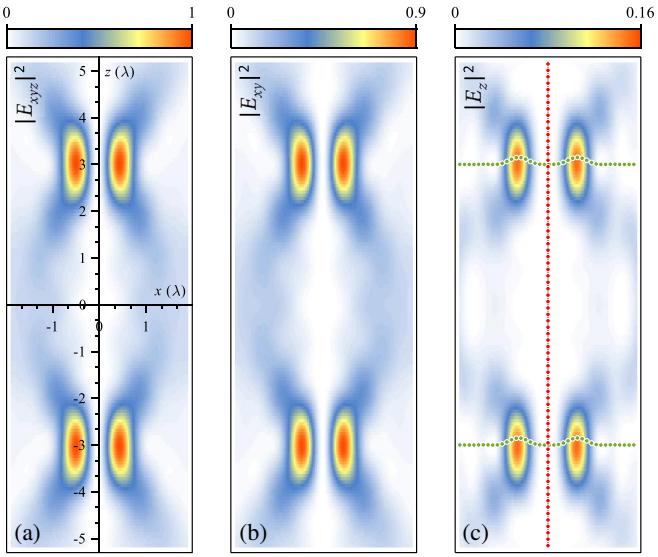

FIG. 2. Simulated electric field intensity distributions of a tightly focused $\mathrm{LG}_{(0,0)}$ input field in the $x - z$ plane when $m = -1$ and $\Delta z = 3\lambda$: (a) total, (b) transverse, and (c) longitudinal field components.

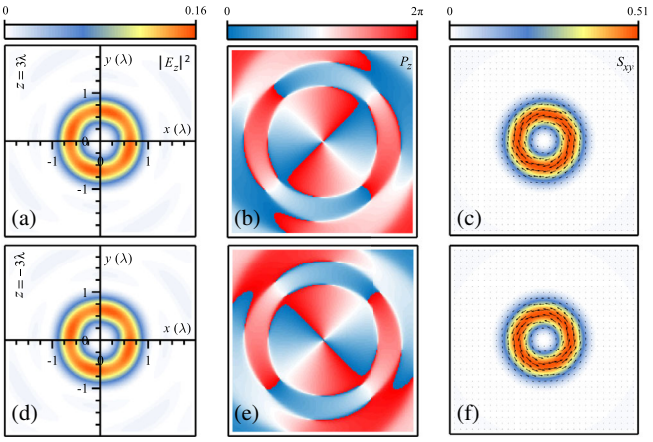

FIG. 3. Simulated electric field intensity and phase distributions of the longitudinal component, as well as the transverse energy flow of tightly focused $LG_{(0,0)}$ beams in the two $x-y$ planes at $z = 3\lambda$ (a)–(c) and -3λ (d)–(f) when $m = -1$ and $\Delta z = 3\lambda$, respectively. (a),(d) Intensity distributions and (b),(e) phase distributions for the longitudinal component. (c),(f) Energy flow of the transverse component (black arrows indicate the direction of flow).

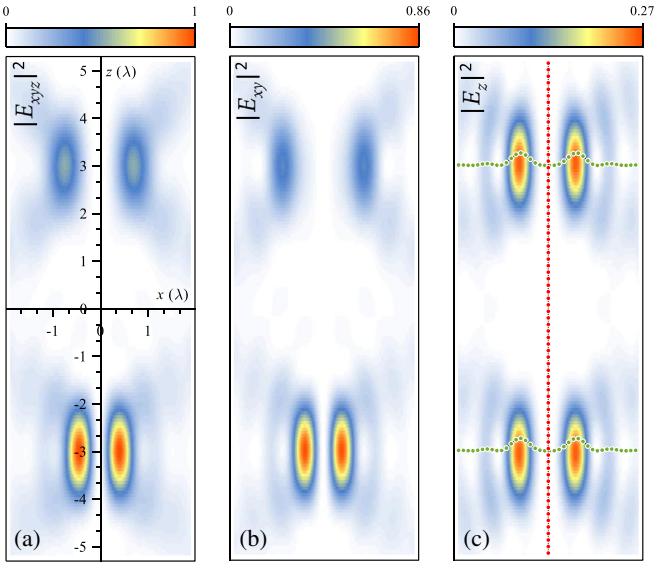

FIG. 4. Simulated electric field intensity distributions of tightly focused $LG_{(2,0)}$ input field in the $x-z$ plane when $m = 1$ and $\Delta z = 3\lambda$: (a) total, (b) transverse, and (c) longitudinal field components.

contributed by the input component of the RH vibration, is located at $(0, 0, 3\lambda)$, whereas for the lower focus, it is located at $(0, 0, -3\lambda)$ and is contributed by the input component of the LH vibration. These results agree with theory very well. We pay special attention to the longitudinal field of light. The corresponding intensity and phase distributions of the longitudinal component and transverse energy flow in the two $x-y$ planes at $z = 3\lambda$ and -3λ are simulated (Fig. 3). The electric field exhibits doughnut-shaped intensity distributions for both the upper [Fig. 3(a)] and lower [Fig. 3(d)] foci and has double clockwise [Fig. 3(e), upper focus, where $\exp[i(l+m-1)\varphi] = \exp(-i2\varphi)]$] and anticlockwise [Fig. 3(e), lower focus, where $\exp[i(l-m+1)\varphi] = \exp(i2\varphi)]$] helical phase distributions. The corresponding transverse energy flows in the two aforementioned $x-y$ planes are calculated [Figs. 3(c) and 3(f)]. Evidently, they are both ring-shaped patterns with the same profiles and magnitude but exhibiting energy flows of opposite direction (black arrows indicate the direction of flow) arising from the opposite helical phases of the longitudinal fields. When particles are trapped at these two locations, they would rotate along different directions in the horizontal xy plane following the transverse energy flow. This also provides a way to observe the creation of conjugate phase vortexes [59].

When another optical DOF of l is introduced, arbitrary independent topologies for the two longitudinal polarization vortex structures can be achieved. To prove this, we consider a $LG_{(2,0)}$ input beam with $\Delta z = 3\lambda$ and $m = 1$ (NA $= 0.95$, $n = 1$). In this case, the two foci should have the same topological charge $l+m-1 = -2$ and $l-m+1 = 2$, which is quite different from the previous case. The simulated electric field intensities in the $x-z$ plane (Fig. 4) show two foci distributions for the total, transverse, and longitudinal fields and are located at $(0, 0, 3\lambda)$ and $(0, 0, -3\lambda)$, respectively. Both foci for the total field exhibit hollow-shaped profiles but of different sizes, which is quite different from the longitudinal component. Similar to Fig. 3, the corresponding intensity and phase distributions of the longitudinal component and transverse energy flow in the two $x-y$ planes at $z = 3\lambda$ and -3λ are studied in detail (Fig. 5). The twin foci exhibit the same

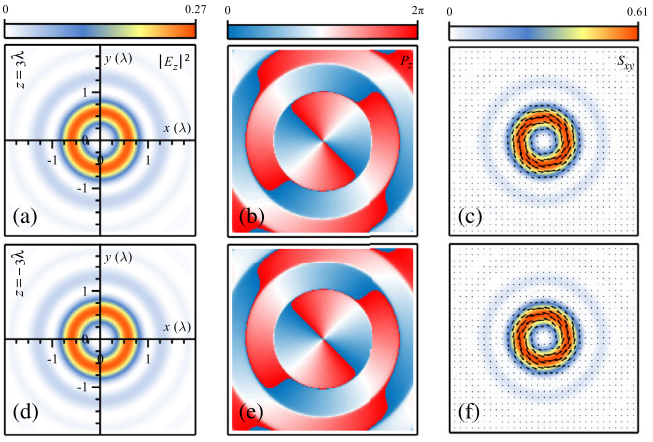

FIG. 5. Simulated electric field intensity and phase distributions of the longitudinal component, as well as the transverse energy flow of tightly focused $LG_{(2,0)}$ beams in the two $x-y$ planes at $z = 3\lambda$ (a)–(c) and -3λ (d)–(f) when $m = 1$ and $\Delta z = 3\lambda$, respectively. (a),(d) Intensity distributions and (b),(e) phase distributions for the longitudinal component. (c),(f) Energy flow of the transverse component (black arrows indicate the direction of flow).

intensity [Fig. 5(a), upper focus; Fig. 5(d), lower focus], phase [Fig. 5(b), upper focus, where $\exp[i(l+m-1)\varphi]=\exp(i2\varphi)$; Fig. 5(e), lower focus, where $\exp[i(l-m+1)\varphi]=\exp(i2\varphi)$], and transverse energy flow [Fig. 5(c), upper focus; Fig. 5(f), lower focus]. Compared with the energy flows in Fig. 3, the energy flows here in the two aforementioned $x-y$ planes have not only the same profiles and magnitude, but also the same flow directions, arising from the same helical phases of the longitudinal fields. This means that, if particles are trapped around the two foci, they would rotate along the same direction in the horizontal xy plane, which further illustrates the powerful capability of manipulation of the longitudinal polarization vortex structures.

In addition to the wide range of academic interest and the huge potential and practical applications, a precise measurement of the refined structure in the longitudinal polarization is a very important topic. Fortunately, advances have been achieved in the probing of the longitudinal field in recent years. The fluorescence of single molecules with fixed absorption dipole orientation were used to probe the longitudinal field strength [60]. Gold nanorings and tip-enhanced near-field microscopes were also applied in detecting the longitudinal field [61,62]. The amplitudes and relative phases of the focal field components can now be reconstructed using a simple measurement scheme that is also straightforward to implement and a reconstruction algorithm based on the scattering signal of a single spherical nanoparticle [63].

In conclusion, we have presented a simple method to realize dual coaxial longitudinal polarization vortices capable of possessing arbitrary independent topological charges, as well as tunable spatial separations between them. We described how to choose the optical DOF of the transverse phase and polarization structures in realizing them. We developed a rigorous analytical model to calculate the electromagnetic field and energy flow in the focal volume of the structured input field we proposed. The application of this method has the potential to broaden the field concerning structured vortices and thereby open discoveries of new techniques in optical manipulation and imaging.

This work was partially supported by National Natural Science Foundation of China (NSFC) (11604182, 11704226).

*These authors contributed equally to this work.
†xcyuan@szu.edu.cn
‡h.p.urbach@tudelft.nl

[1] V. B. Berestetskii, E. M. Lifshitz, and L. P. Pitaevskii, *Quantum Electrodynamics, Course of Theoretical Physics* (Butterworth-Heinemann, Oxford, 1982), Vol. 4.
[2] S. M. Barnett and L. Allen, Opt. Commun. **110**, 670 (1994).
[3] J. H. Poynting, Proc. R. Soc. A **82**, 560 (1909).
[4] R. A. Beth, Phys. Rev. **50**, 115 (1936).
[5] L. Allen, M. W. Beijersbergen, R. J. C. Spreeuw, and J. P. Woerdman, Phys. Rev. A **45**, 8185 (1992).
[6] L. Allen, M. J. Padgett, and M. Babiker, Prog. Opt. **39**, 291 (1999).
[7] A. T. O'Neil, I. MacVicar, L. Allen, and M. J. Padgett, Phys. Rev. Lett. **88**, 053601 (2002).
[8] M. Padgett, J. Courtial, and L. Allen, Phys. Today **57**, No. 5, 35 (2004).
[9] G. Molina-Terriza, J. P. Torres, and L. Torner, Nat. Phys. **3**, 305 (2007).
[10] S. Franke-Arnold, L. Allen, and M. Padgett, Laser Photonics Rev. **2**, 299 (2008).
[11] A. M. Yao and M. J. Padgett, Adv. Opt. Photonics **3**, 161 (2011).
[12] K. Y. Bliokh and F. Nori, Phys. Rep. **592**, 1 (2015).
[13] M. J. Padgett, Opt. Express **25**, 11265 (2017).
[14] J. F. Nye and M. V. Berry, Proc. R. Soc. A **336**, 165 (1974).
[15] V. Yu. Bazhenov, M. V. Vasnetsov, and M. S. Soskin, JETP Lett. **52**, 429 (1990), http://www.jetpletters.ac.ru/ps/1159/article_17529.pdf.
[16] D. G. Grier, Nature (London) **424**, 810 (2003).
[17] L. Paterson, M. P. MacDonald, J. Arlt, W. Sibbett, P. E. Bryant, and K. Dholakia, Science **292**, 912 (2001).
[18] G. Gibson, J. Courtial, M. J. Padgett, M. Vasnetsov, V. Pas'ko, S. M. Barnett, and S. Franke-Arnold, Opt. Express **12**, 5448 (2004).
[19] C. Paterson, Phys. Rev. Lett. **94**, 153901 (2005).
[20] J. Wang, J. Yang, I. M. Fazal, N. Ahmed, Y. Yan, H. Huang, Y. Ren, Y. Yue, S. Dolinar, M. Tur, and A. E. Willner, Nat. Photonics **6**, 488 (2012).
[21] A. E. Willner, H. Huang, Y. Yan, Y. Ren, N. Ahmed, G. Xie, C. Bao, L. Li, Y. Cao, Z. Zhao, J. Wang, M. P. J. Lavery, M. Tur, S. Ramachandran, A. F. Molisch, N. Ashrafi, and S. Ashrafi, Adv. Opt. Photonics **7**, 66 (2015).
[22] J. Wang, Photonics Res. **4**, B14 (2016).
[23] N. Bozinovic, Y. Yue, Y. Ren, M. Tur, P. Kristensen, H. Huang, A. E. Willner, and S. Ramachandran, Science **340**, 1545 (2013).
[24] S. W. Hell and J. Wichmann, Opt. Express **19**, 780 (1994).
[25] S. W. Hell, Science **316**, 1153 (2007).
[26] S. W. Hell, Nat. Biotechnol. **21**, 1347 (2003).
[27] A. R. Altman, K. G. Köprülü, E. Corndorf, P. Kumar, and G. A. Barbosa, Phys. Rev. Lett. **94**, 123601 (2005).
[28] J. Leach, B. Jack, J. Romero, A. K. Jha, A. M. Yao, S. Franke-Arnold, D. G. Ireland, R. W. Boyd, S. M. Barnett, and M. J. Padgett, Science **329**, 662 (2010).
[29] M. W. Beijersbergen, R. P. C. Coerwinkel, M. Kristensen, and J. P. Woerdman, Opt. Commun. **112**, 321 (1994).
[30] S. S. R. Oemrawsingh, J. A. W. van Houwelingen, E. R. Eliel, J. P. Woerdman, E. J. K. Verstegen, J. G. Kloosterboer, and G. W. 't Hooft, Appl. Opt. **43**, 688 (2004).
[31] K. Sueda, G. Miyaji, N. Miyanaga, and M. Nakatsuka, Opt. Express **12**, 3548 (2004).
[32] V. V. Kotlyar, A. A. Almazov, S. N. Khonina, and V. A. Soifer, J. Opt. Soc. Am. A **22**, 849 (2005).
[33] N. R. Heckenberg, R. McDuff, C. P. Smith, and A. G. White, Opt. Lett. **17**, 221 (1992).
[34] B. Terhalle, A. Langner, B. Päivänranta, V. A. Guzenko, C. David, and Y. Ekinci, Opt. Lett. **36**, 4143 (2011).
[35] G. Binener, A. Niv, V. Kleiner, and E. Hasman, Opt. Lett. **27**, 1875 (2002).

[36] L. Marrucci, C. Manzo, and D. Paparo, Phys. Rev. Lett. **96**, 163905 (2006).
[37] E. Karimi, S. A. Schulz, I. De Leon, H. Qassim, J. Upham, and R. W. Boyd, Light Sci. Appl. **3**, e167 (2014).
[38] L. Marrucci, E. Karimi, S. Slussarenko, B. Piccirillo, E. Santamato, E. Nagali, and F. Sciarrino, J. Opt. **13**, 064001 (2011).
[39] K. Y. Bliokh, E. A. Ostrovskaya, M. A. Alonso, O. G. Rodriguez-Herrera, D. Lara, and C. Dainty, Opt. Express **19**, 26132 (2011).
[40] F. Manni, K. G. Lagoudakis, T. K. Paraïso, R. Cerna, Y. Léger, T. C. H. Liew, I. A. Shelykh, A. V. Kavokin, F. Morier-Genoud, and B. Deveaud-Plédran, Phys. Rev. B **83**, 241307(R) (2011).
[41] E. Karimi, L. Marrucci, V. Grillo, and E. Santamato, Phys. Rev. Lett. **108**, 044801 (2012).
[42] J. Zhu, Y. Chen, Y. Zhang, X. Cai, and S. Yu, Opt. Lett. **39**, 4435 (2014).
[43] K. Y. Bliokh, F. J. Rodríguez-Fortuño, F. Nori, and A. V. Zayats, Nat. Photonics **9**, 796 (2015).
[44] F. Cardano and L. Marrucci, Nat. Photonics **9**, 776 (2015).
[45] R. C. Devlin, A. Ambrosi, D. Wintz, S. L. Oscurato, A. Y. Zhu, M. Khorasaninejad, J. Oh, P. Maddalena, and F. Capasso, Opt. Express **25**, 377 (2017).
[46] R. C. Devlin, A. Ambrosil, N. A. Rubin, J. P. B. Mueller, and F. Capasso, Science **358**, 896 (2017).
[47] A K. S. Youngworth and T. G. Brown, Opt. Express **7**, 77 (2000).
[48] R. Dorn, S. Quabis, and G. Leuchs, Phys. Rev. Lett. **91**, 233901 (2003).
[49] F. Maucher, S. Skupin, S. A. Gardiner, and I. G. Hughes, Phys. Rev. Lett. **120**, 163903 (2018).
[50] H. Wang, L. Shi, B. Lukyanchuk, C. Sheppard, and C. T. Chong, Nat. Photonics **2**, 501 (2008).
[51] Y. Zhao, J. S. Edgar, G. D. M. Jeffries, D. McGloin, and D. T. Chiu, Phys. Rev. Lett. **99**, 073901 (2007).
[52] C. Maurer, A. Jesacher, S. Fürhapter, S. Bernet, and M. Ritsch-Marte, New J. Phys. **9**, 78 (2007).
[53] Q. Zhan, Adv. Opt. Photonics **1**, 1 (2009).
[54] A. Arbabi, Y. Horie, M. Bagheri, and A. Faraon, Nat. Nanotechnol. **10**, 937 (2015).
[55] J. P. Balthasar Mueller, N. A. Rubin, R. C. Devlin, B. Groever, and F. Capasso, Phys. Rev. Lett. **118**, 113901 (2017).
[56] S. Pancharatnam, Proc. Indian Acad. Sci. A **44**, 247 (1956).
[57] M. V. Berry, J. Mod. Opt. **34**, 1401 (1987).
[58] B. Richards and E. Wolf, Proc. R. Soc. A **253**, 358 (1959).
[59] H. He, M. E. J. Friese, N. R. Heckenberg, and H. Rubinsztein-Dunlop, Phys. Rev. Lett. **75**, 826 (1995).
[60] L. Novotny, M. R. Beversluis, K. S. Youngworth, and T. G. Brown, Phys. Rev. Lett. **86**, 5251 (2001).
[61] N. Hayazawa, Y. Saito, and S. Kawata, Appl. Phys. Lett. **85**, 6239 (2004).
[62] J. Fulmes, D. A. Gollmer, S. Jäger, C. Schäfer, A. Horrer, D. Zhang, P.-M. Adam, A. J. Meixner, D. P. Kern, and M. Fleischer, Opt. Express **26**, 14982 (2018).
[63] T. Bauer, S. Orlov, U. Peschel, P. Banzer, and G. Leuchs, Nat. Photonics **8**, 23 (2014).